

Muhammad Hassan
Asghar¹
Philipp Brockmann²
Xulan Dong²
Matthias Niethammer¹
Tomislav Maric¹
Ilia Roisman³
Dieter Bothe^{1,*}


Asymmetry During Fast Stretching of a Liquid Bridge

The dynamics of an axisymmetric liquid bridge stretch are investigated by means of numerical simulations, and the results are validated experimentally. The constant acceleration of the lower substrate stretches the liquid bridge. A simplified simulation model of the experimental setup is developed for the unstructured volume-of-fluid two-phase flow simulation method, which models the lower substrate as a fluid with a prescribed constant acceleration of the retracting substrate. The effect of stretching acceleration, fluid properties, and liquid volume on the liquid bridge dynamics is investigated. It is shown that at low acceleration the length of the lower portion of the bridge is greater than the upper portion, which is reversed at high acceleration. With increasing viscosity, this effect is decreased and the bridge becomes more symmetric.

Keywords: Asymmetric stretching experiment, Axisymmetric liquid bridge stretch, Liquid bridges, Unstructured volume-of-fluid method

Received: May 15, 2023; *accepted:* June 22, 2023

DOI: 10.1002/ceat.202300240

 This is an open access article under the terms of the Creative Commons Attribution License, which permits use, distribution and reproduction in any medium, provided the original work is properly cited.

1 Introduction

Liquid bridge stretching refers to the behavior of a liquid bridge, which is a thin column of liquid connecting two solid surfaces [1], and its exploration goes back to the works of Rayleigh [2] and Stefan [3] over a hundred years ago. Liquid bridge stretching is a phenomenon that occurs when an external force is applied to the solid surfaces, causing the bridge to elongate. As the bridge stretches, the diameter of the bridge decreases due to the larger bridge length. Hence, the effect of surface tension -increases, resulting in a vase-like structure, as shown in Fig. 1. The stretching of the liquid bridge occurs due to the balance between surface tension and the force applied to the retracting substrate. This has been extensively studied in the field of fluid mechanics by Kumar [4], Brulin et al. [5,6], and Brulin [7]. Liquid bridge stretching has been investigated both experimentally and theoretically, with several models proposed to describe the behavior, e.g., by Zhang et al. [1] and Brulin [7].

Liquid bridges can occur in a variety of industrial processes. In the printing industry, liquid bridges can be formed between the surface being coated and the roller, potentially affecting the quality of the prints as reported by Kumar et al. [4], Brumm et al. [8], and Brumm et al. [9]. Also, in inkjet printing technology, liquid bridges are encountered during the printing process; see Hoath et al. [10]. In the food and beverage industry, liquid bridges can occur during the processing and packaging of products such as sauces, jams, juices, or food powders, affecting the quality and consumer perception of the final product as described by Adhikari et al. [11], Dhanalakshmi et al. [12], Jimenez et al. [13], and Wei et al. [14].

Moreover, comprehending and predicting the pinch-off phenomenon of liquid bridges holds significant importance in drug delivery and microdispersion applications, as it facilitates the precise and efficient dispensing of liquid volumes; see Chen et al. [15]. The stretching of non-Newtonian fluids can also be used for rheological measurements of complex fluids as found by McKinley et al. [16].

In addition to experimental and theoretical studies, numerical investigations of liquid bridge stretching have yielded valuable insights into the phenomenon. Zhuang and Ju [17] studied the deformation of axisymmetric liquid bridges using the arbitrary Lagrangian-Eulerian (ALE) [18] method for stretching velocity up to 3 m s^{-1} . They observed increased bridge length at the necking with higher stretching velocity. They noted that the amount of liquid left at the stationary plate after the breakup rises with increasing stretching velocity. Dodds et al. [19] studied the effect of contact line dynamics on the amount of liquid left on the substrates using the 2D Galerkin FEM method in Stokes flow. They also investigated the effect of substrate geom-

¹Muhammad Hassan Asghar, Dr. Matthias Niethammer, Dr.-Ing. Tomislav Maric, Prof. Dr. Dieter Bothe (bothe@mma.tu-darmstadt.de) TU Darmstadt, Mathematical Modeling and Analysis, Peter-Grünberg-Strasse 10, 64287 Darmstadt, Germany.

²Dr.-Ing. Philipp Brockmann, Xulan Dong TU Darmstadt, Institute of Fluid Mechanics and Aerodynamics, Flughafenstrasse 19, 64347 Griesheim, Germany.

³Prof. Dr. Ilia Roisman TU Darmstadt, Institute of Fluid Mechanics and Aerodynamics, Peter-Grünberg-Strasse 10, 64287 Darmstadt, Germany.

etry on the breakup dynamics and observed that the pinning of the contact line in the substrate cavity governs the liquid transfer onto the substrates. Gaudet et al. [20] analyzed the effect of capillary number and fluid viscosity on liquid bridge dynamics using the boundary integral method. They showed that less viscous liquids and stretching at lower capillary number results in shorter bridge length before the breakup.

The present study aims to quantitatively analyze the competition between viscous and inertial effects on the symmetry of a liquid bridge during the early stretching stage. The insights of the symmetry investigation could effectively control the amount of leftover volume at each substrate which is vital in printing and drug delivery. The symmetry of the liquid bridge stretch is defined by the symmetry factor, defined as

$$S = \frac{L}{U} \quad (1)$$

where L and U are the distance of the lower and upper substrates from the necking, respectively, as illustrated in Fig. 1. Moreover, the study aims to capture the liquid bridge stretching dynamics with simplified boundary conditions, where the lower substrate is modeled by imposing a velocity given by the acceleration of the retracted substrate onto a fluid base of the liquid bridge, significantly reducing the complexity of the computation. A combined numerical and experimental study is performed, covering low and high acceleration values, viscosity, and Ohnesorge number ($Oh = \mu/\sqrt{\rho R \dot{\sigma}}$). For all parametric case studies, the input data, the secondary data and the post-processing utilities are publicly available online [37–39].

For numerical simulations, the ESI OpenFOAM [21] version (git tag OpenFOAM-v2212) [22] is used. The solver interFlow [23, 24] from the TwoPhaseFlow OpenFOAM library [24] is applied, which employs the plicRDF-isoAdvector method [25, 26].

2 Experimental Setup

All experiments performed in this study are based on a rapidly stretched liquid bridge formed between two horizontally aligned substrates (see Fig. 2). The upper substrate remains fixed, and the motion of the lower substrate induces the stretching process.

The main component of the stretching apparatus is the linear drive (Akrabis, type SGL100-AUM3), which is regulated by a servo controller (Metronix, ARS2108). This linear unit provides accelerations up to 180 ms^{-2} reliably [7, 27], and achieves a peak force of 900 N and a positioning accuracy of $5 \mu\text{m}$ [7]. Two separate high-speed video systems are utilized for observation. The first high-speed camera (Photron SA X2 (1)) records the liquid bridge from the top through the transparent upper substrate. A coaxial illumination is realized with a high-power LED (2) and a beam splitter, which is implemented in a Navitar Zoom Objective (3).

The images generated with a high-speed camera (1) are used to ensure that the droplet is not skewed during the experiment. The second high-speed camera (Phantom Miro Lab 110 (7)) with a pixel size of $20 \times 20 \mu\text{m}$ records the side profile using a telecentric objective (6) and a telecentric white light LED (4). The images generated with this camera are used to extract the liquid bridge contours. The camera is operated at 6200 fps and

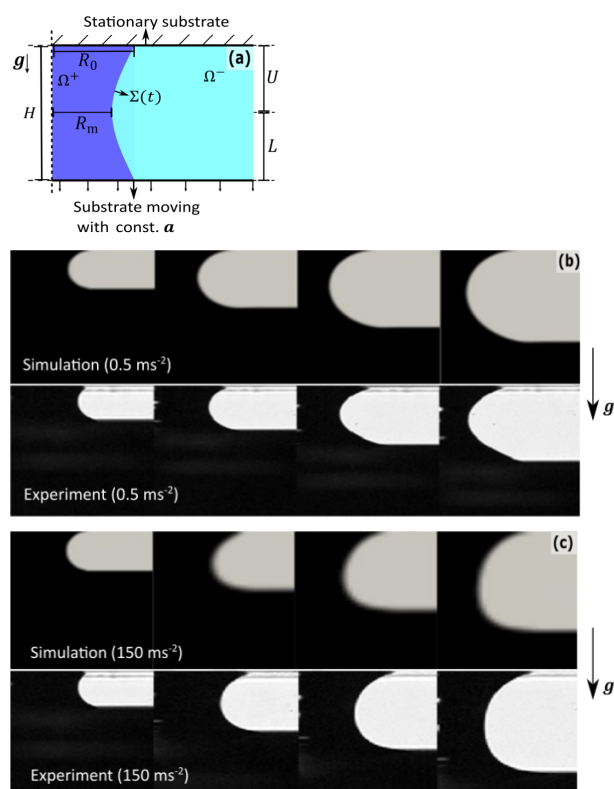


Figure 1. (a) Schematic diagram of the liquid bridge stretching ($\Omega^+(t)$: liquid, and $\Omega^-(t)$: air). The upper substrate is stationary, while the lower substrate is moved with constant acceleration. The gravitational acceleration acts in a downward direction. The contact line is pinned having the foot radius R_0 of the liquid bridge at the stationary substrate, the bridge neck radius is R_m , and the height of the liquid bridge is H . L and U are the lengths of the lower and upper portion, respectively. (b) and (c) present the numerical and experimental profiles of the liquid bridge stretching for Gly70, volume $V = 10 \mu\text{L}$, and accelerations of 0.5 ms^{-2} and 150 ms^{-2} , respectively. In (b), the symmetry factor S (Eq. (1)) is greater than 1, whereas in (c) S is less than 1.

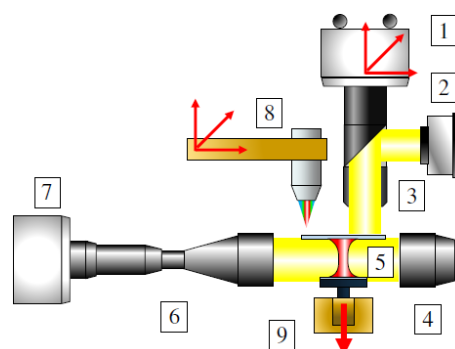


Figure 2. Schematic of the experiment setup. (1) High-speed camera on a traverse, (2) LED, (3) objective, (4) LED, (5) liquid bridge, (6) telecentric objective, (7) high-speed camera, (8) confocal sensor on a traverse, (9) linear actuator.

a resolution of $512 \times 512 \text{ px}$, covering a field of view of $13.5 \times 13.5 \text{ mm}$.

To ensure a parallel orientation of the two substrates, the distance between the substrates is checked with a confocal sensor with an accuracy of 3 nm (Micro Epsilon IFS2407-0.1 (2)). To prepare the experiment, the bottom substrate is lowered. The droplet is applied on the lower substrate by a syringe pump equipped with an insulin syringe (1 mL, SFM GmbH), connected to a custom-built needle holder. After applying the droplet, the needle holder is removed, and the lower substrate is raised to form a liquid bridge.

Four different liquids are used to investigate the influence of viscosity and surface tension. Their properties are listed in Tab. 1. A ternary mixture of 26.46 wt % water, 32.30 wt % glycerol, and 41.24 wt % ammonium thiocyanate is used as an intermediate viscosity liquid and is abbreviated as RIM [28]. The surface tension was measured with a DataPhysics DCAT tensiometer as $\sigma = 49 \text{ mN m}^{-1}$. Distilled water is used as a low-viscosity liquid with fluid properties taken from the literature [29,30]. A 70 wt % glycerol water solution was utilized as a high-viscosity liquid. The viscosity and density were calculated based on the works of Cheng [31] and Volk and Kähler [32], and the surface tension was determined based on the work of Takamura et al. [33]. Finally, pure glycerol is employed. The fluid parameters are listed in Tab. 1.

Table 1. Properties of fluids: RIM, DW (distilled water), water-glycerol (70 wt % glycerol, water mixture), and glycerol.

Fluid	μ [kg m ⁻¹ s ⁻¹]	σ [N m ⁻¹]	ρ [kg m ⁻³]
RIM	4.99×10^{-3}	49×10^{-3}	1190
DW	9×10^{-4}	71.8×10^{-3}	997
Water-glycerol (Gly70)	2.31×10^{-2}	66×10^{-3}	1180.7
Glycerol	1.4138	63.4×10^{-3}	1260.8

The MATLAB Image Processing Toolbox is taken to extract droplet contours from side-view grayscale images. For this, the images are binarized using the “imbinarize” function with no additional parameters. The resulting binarized image is then inverted using “imcomplement”, and the boundaries are extracted with the “bwboundaries” function. With the boundaries detected, other properties, like the neck radius, can easily be extracted.

3 Numerical Method and Computational Domain

The plicRDF isoAdvector method [25,26] is used to simulate liquid bridge dynamics in an axisymmetric computational (wedge) setup. The plicRDF-isoAdvector method is an unstructured volume-of-fluid (VOF) method (see [34] for a recent review and [35] for wetting test cases) implemented in OpenFOAM. This section provides an overview of the numerical method and the computational setup.

3.1 VOF Method

Consider a physical domain Ω as illustrated in Fig. 1, composed of two sub-domains filled with different incompressible fluids, denoted by $\Omega^+(t)$ and $\Omega^-(t)$. The sub-domains Ω^\pm are distinguished by the phase indicator function:

$$\chi(t, \mathbf{x}) = \begin{cases} 1, & \mathbf{x} \in \Omega^+(t) \\ 0, & \mathbf{x} \notin \Omega^+(t) \end{cases} \quad (2)$$

The volume fraction $\alpha_c(t)$ of the phase $\Omega^+(t)$ within a control volume Ω_c at time t is defined as:

$$\alpha_c(t) = \frac{1}{|\Omega_c|} \int_{\Omega_c} \chi(t, \mathbf{x}) dV \quad (3)$$

The presence of the phase $\Omega^+(t)$ inside a cell is indicated by the volume fraction. Indeed, it holds that

$$\begin{aligned} \alpha_c = 1 &\leftrightarrow \text{cell is inside } \Omega^+(t) \\ \alpha_c \in (0, 1) &\leftrightarrow \text{cell intersects the interface } \Sigma(t) \\ \alpha_c = 0 &\leftrightarrow \text{cell is inside } \Omega^-(t) \end{aligned} \quad (4)$$

Within each phase $\Omega^+(t)$ or $\Omega^-(t)$, the continuity equation for incompressible flows has the form of:

$$\nabla \cdot \mathbf{v} = 0 \quad (5)$$

where \mathbf{v} is the fluid velocity. For two-phase flows without phase change, the phase indicator function keeps its value along trajectories of the two-phase flow, i.e., it satisfies (in a distributional sense) the transport equation:

$$\partial_t \chi + \mathbf{v} \cdot \nabla \chi = 0 \quad (6)$$

The phase-indicator $\chi(t, \cdot)$ determines the phase-dependent local values of the physical quantities, such as the single-field density ρ and viscosity μ in the single-field formulation of the two-phase Navier Stokes equations. For constant densities ρ^\pm , ρ and constant viscosities μ^\pm , μ , it follows:

$$\begin{aligned} \rho(t, \mathbf{x}) &= \chi(t, \mathbf{x})\rho^+ + (1 - \chi(t, \mathbf{x}))\rho^- \\ \mu(t, \mathbf{x}) &= \chi(t, \mathbf{x})\mu^+ + (1 - \chi(t, \mathbf{x}))\mu^- \end{aligned} \quad (7)$$

The momentum balance reads as:

$$\begin{aligned} \partial_t(\rho \mathbf{v}) + \nabla \cdot (\rho \mathbf{v} \mathbf{v}) = \\ - \nabla p' - \nabla(\rho \mathbf{g} \cdot \mathbf{x}) + \nabla \cdot (\mu(\nabla \mathbf{v} + \nabla \mathbf{v}^T)) + \mathbf{f}_\Sigma \end{aligned} \quad (8)$$

where $p' = p - (\rho \mathbf{g} \cdot \mathbf{x})$ is the modified pressure, \mathbf{g} is the gravitational acceleration, and $\mathbf{f}_\Sigma = \sigma \kappa \mathbf{n}_\Sigma \delta_\Sigma$.

Within the VOF method [34], Eq. (6) is integrated over a fixed control volume Ω_c within a time interval $[t^n, t^{n+1}]$. The application of the Reynolds transport theorem and the decomposition of the cell boundary $\partial \Omega_c = \cup_{f \in F_c} S_f$ leads to the integral form of the volume fraction transport equation (see [34] for details), which reads as:

$$\begin{aligned} \alpha_c(t^{n+1}) &= \alpha_c(t^n) - \frac{1}{|\Omega_c|} \sum_{f \in F_c} \int_{t^n}^{t^{n+1}} \int_{S_f} \chi(t, \mathbf{x}) \mathbf{v} \cdot \mathbf{n} dS dt \\ &= \alpha_c(t^n) - \frac{1}{|\Omega_c|} \sum_{f \in F_c} V_f^\alpha \end{aligned} \quad (9)$$

where V_f^α is the amount of the phase-specific volume fluxed over the face S_f within a time interval $[t^n, t^{n+1}]$.

3.2 The isoAdvecting Advection Scheme

The isoAdvecting numerical method [25] allows to calculate the phase-specific fluxed volume V_f^α by evaluating the instantaneous face area:

$$A_f(t)dt = \int_{S_f} \chi(t, \mathbf{x}) dS dt \quad (10)$$

submerged in $\Omega^+(t)$ at time t . Details on the geometrical evaluation of the $A_f(t)$ are available in [25]; see also [35].

3.3 The plicRDF Reconstruction Scheme

The plicRDF reconstruction scheme [26] is an iterative variant of the reconstructed signed distance function (RDF) method [36], for estimation of the initial interface normal using the piecewise linear interface calculation (PLIC) algorithm. The plicRDF method improves the initial interface normal orientation iteratively by reconstructing the so-called signed distance function ψ_c in the center of the cell Ω_c (cf. Fig. 3) and updates the approximated interface normals $\mathbf{n}_{\Sigma, c}$ as:

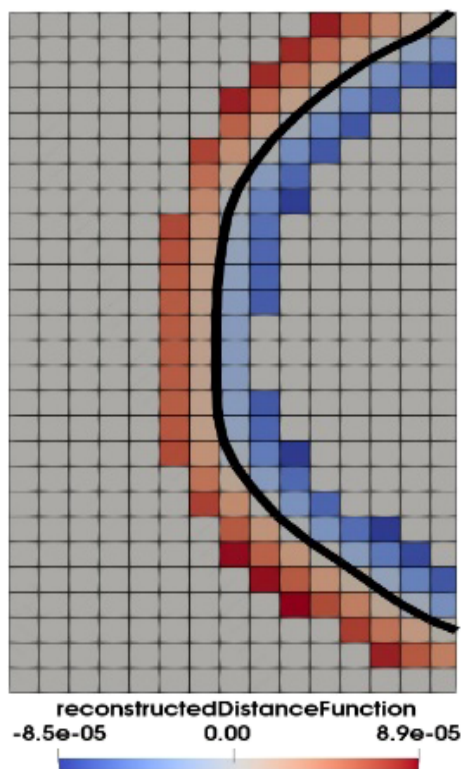


Figure 3. Reconstructed signed distance function field for contour of a liquid bridge.

$$\mathbf{n}_{\Sigma, c}^{k+1} = \frac{\nabla_c \psi_c^k}{\|\nabla_c \psi_c^k\|} \quad (11)$$

where $k = 1, \dots, 5$ is used in [26], and ∇_c is the discrete unstructured finite volume least squares gradient.

3.4 Computational Setup

An axisymmetric liquid bridge is simulated for the validation study. A fluid is confined between two parallel substrates surrounded by air, as illustrated in Fig. 4.

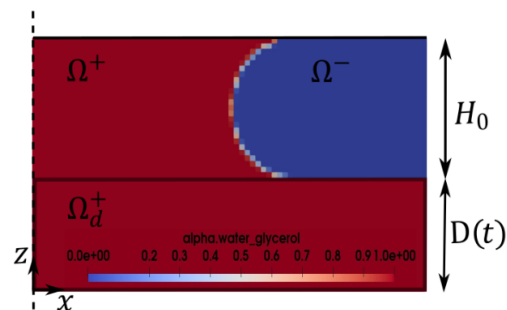


Figure 4. Computational domain (wedge), $\Omega^+(t)$: liquid bridge, $\Omega^-(t)$: air, and $\Omega_d^+(t)$: sub-domain used to model the lower substrate. $\Omega_d^+(t)$ is the domain portion where the velocity field \mathbf{v}_d^+ is assigned at every time step.

3.4.1 Boundary Conditions

At the upper substrate:

The domain boundary $\partial\Omega$ is assumed to be impermeable, i.e.,

$$\mathbf{v}_\perp|_{\partial\Omega} = 0 \quad (12)$$

where \mathbf{v}_\perp is the velocity component normal to the domain boundary. The no-slip boundary condition, i.e.,

$$\mathbf{v}_\parallel|_{\partial\Omega} = 0 \quad (13)$$

together with impermeability condition is applied at the upper substrate.

At the lower substrate:

The liquid bridge is stretched using constant acceleration \mathbf{a} in the $-z$ direction. In this study, the bottom substrate is modeled by imposing the flow field $\mathbf{v}_d^+ = \mathbf{a} \cdot t$ at every time step in the region:

$$\Omega_d^+(t) = \mathbf{x} \in \Omega : \mathbf{x} \leq D(t) \quad (14)$$

where the instantaneous height $D(t)$ of the domain $\Omega_d^+(t)$ at a time t is given by the kinematic condition:

$$D(t) = \frac{\mathbf{a}t^2}{2} + D_0 \quad (15)$$

where D_0 is the initial height of the domain $\Omega_d^+(t)$. The updated velocity field is then given to the pressure velocity cou-

pling algorithm, which ensures the divergence-free nature of the velocity field. This modeling methodology significantly reduces the complexity of the problem, otherwise present in the dynamic mesh motion or layer addition/removal strategy typically applied to the considered problem in the context of Eulerian two-phase flow simulation methods. The stretching methodology is summarized in Algorithm 1.

Algorithm 1: Update the velocity field

```

initialize the current simulation time, acceleration
compute the updated velocity  $v_d^*$  and height  $h_s(t)$ 
for a fixed number of outer iterations do
  for cells do
    if the cell is not an interface cell then
      if the cell center is below the updated height then
        mark cell: updated cell
        update the cell-centered velocity with  $v_d^*$ 
      end if
    end if
  end for
discretize the momentum equation
for a fixed number of inner iterations do
  solve the pressure equation
  update the flux field from the updated pressure
end for
end for
    
```

4 Results and Discussion

The governing dimensionless groups used are: (1) Ohnesorge number $Oh = \mu / \sqrt{\rho R_0 \sigma}$, (2) capillary number $Ca = \mu v / \sigma$, and (3) Reynolds number $Re = \rho a^{1/2} k^{1/2} R_0^{3/2} / \mu$.

The evolution of the liquid bridge profile for initial droplet volume $5 \mu\text{L}$ and $10 \mu\text{L}$ for high acceleration (high Re) is investigated first. Figs. 5 and 6 compare the liquid bridge contour obtained from the numerical simulations and experiments, revealing excellent agreement between the two sets of results.

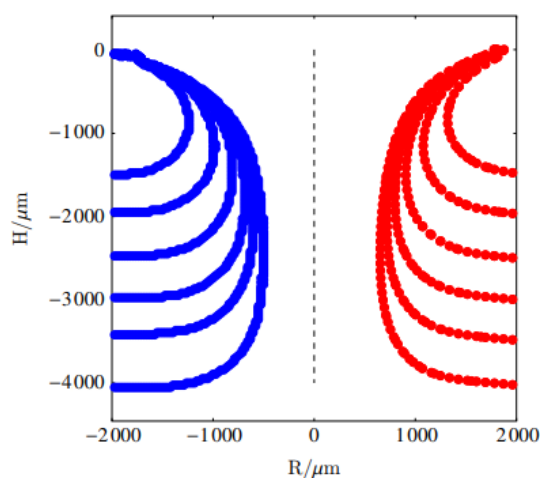


Figure 5. Comparison of the liquid bridge profile at different dimensionless instantaneous bridge heights H/H_0 for fluid Gly70, $V = 10 \mu\text{L}$, $a = 150 \text{ m s}^{-2}$. Red: simulation results, blue: experimental results.

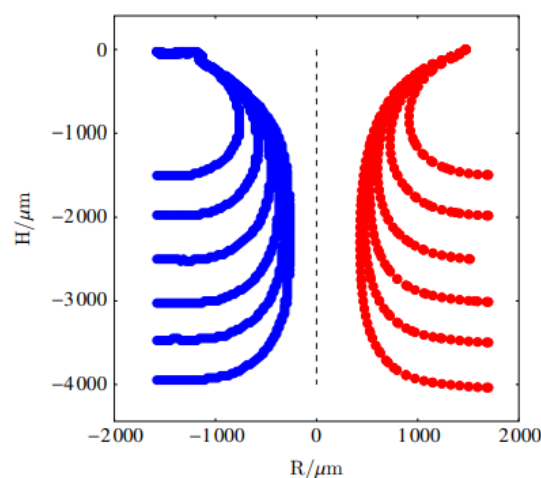


Figure 6. Comparison of the liquid bridge profile at different dimensionless instantaneous bridge heights H/H_0 for fluid Gly70, $V = 5 \mu\text{L}$, $a = 150 \text{ m s}^{-2}$. Red: simulation results, blue: experimental results.

For low Reynolds numbers, the numerical simulation deviates from the experimental results at the later stages of stretching as shown in Figs. 7 and 8. At low Re and relatively thin neck diameters, surface tension effects are stronger than inertial effects. The presented simplified numerical model for the lower substrate underestimates these effects at low Reynolds numbers. The experiment is close to breakup at $H/H_0 > 3$ (see Figs. 7 and 10). The breakup happens at the neck's lower end, causing asymmetry in the liquid bridge profile. This effect still needs to be captured by the simplified model; hence, the simulation profile (see Fig. 7) is still symmetric.

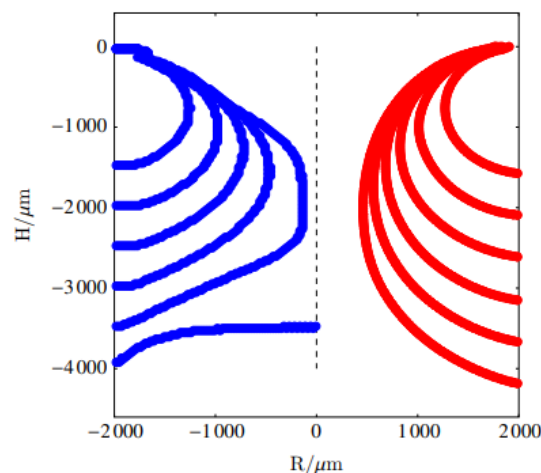


Figure 7. Comparison of the liquid bridge profile at different dimensionless instantaneous bridge heights H/H_0 for fluid RIM, $V = 10 \mu\text{L}$, $a = 5 \text{ m s}^{-2}$. Red: simulation results, blue: experimental results.

The evolution of the neck radius for the *early* stretching stage as a function of the dimensionless instantaneous bridge height H/H_0 is shown in Figs. 8 and 9. Fig. 9 demonstrates the

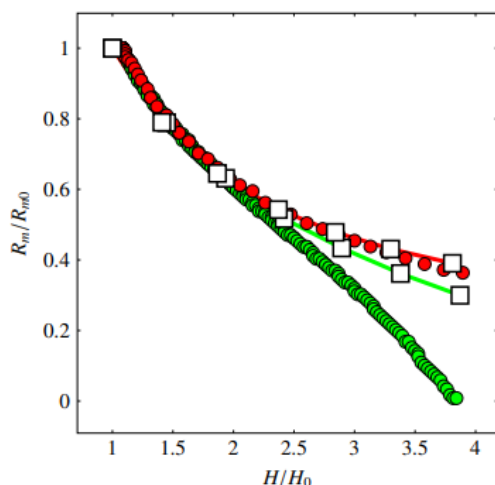


Figure 8. Evolution of the neck radius as a function of the dimensionless instantaneous bridge heights H/H_0 . Gly70, $V = 10 \mu\text{L}$. Green: $Re = 4.675$, red: $Re = 27.59$. \square Simulation results, \circ experimental results.

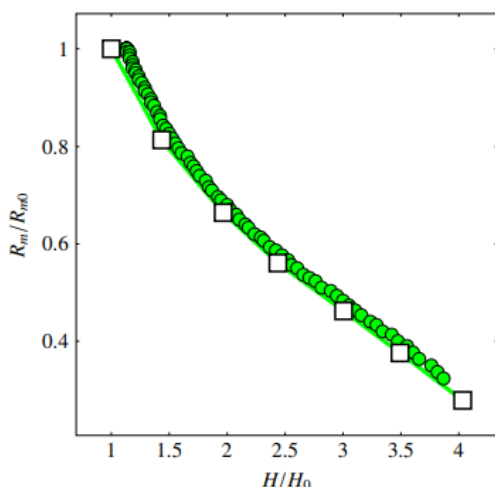


Figure 9. Evolution of the neck radius as a function of the dimensionless instantaneous bridge heights H/H_0 for RIM, $V = 50 \mu\text{L}$. $Re = 11.49$, $a = 0.25 \text{ m s}^{-2}$. \square Simulation results, \circ experimental results.

evolution at the lowest considered acceleration, i.e., 0.25 m s^{-2} , applied on a liquid bridge of volume $50 \mu\text{L}$, and a very good agreement with the experimental result is observed. Fig. 9 indicates that the simplified model can also handle low acceleration at larger volumes.

4.1 Investigation of the Symmetric Stretch of the Liquid Bridge

One of the key features of the liquid bridge stretching dynamics is the symmetry of the liquid bridge. At low acceleration, the lower portion of the bridge contains more volume than the upper portion. With an increase in acceleration, this effect is re-

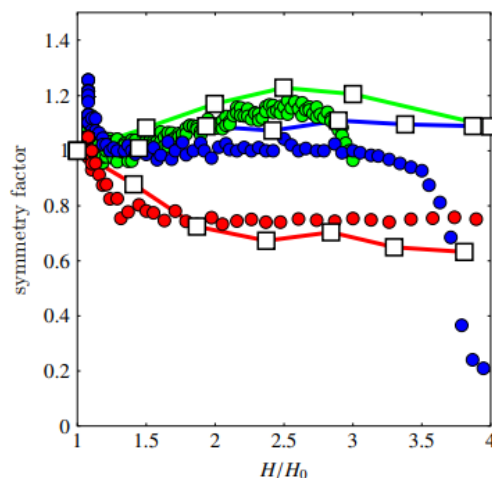


Figure 10. Symmetry factor S for different accelerations. Gly70, $V = 10 \mu\text{L}$. Different colors correspond to different accelerations. Green: 0.5 m s^{-2} , blue: 5 m s^{-2} , red: 150 m s^{-2} . \square Simulation results, \circ experimental results.

versed, as displayed in Fig. 10. The respective liquid bridge profiles for $a = 0.5 \text{ m s}^{-2}$ and $a = 150 \text{ m s}^{-2}$ are presented in Fig. 1. The choice of the liquid also influences the symmetry of the liquid bridge. The asymmetry of the liquid bridge stretch decreases with increasing viscosity, as illustrated in Fig. 11.

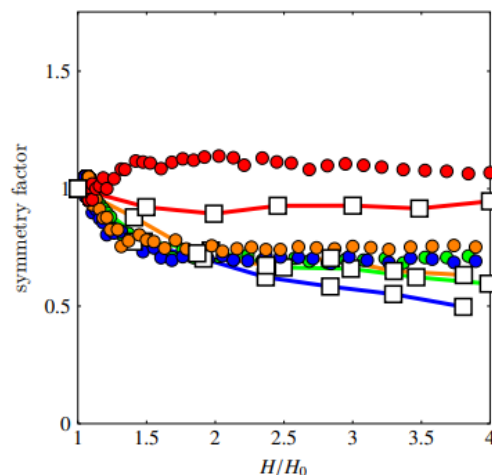


Figure 11. Symmetry factor S for different fluids. $V = 10 \mu\text{L}$, $a = 150 \text{ m s}^{-2}$. Different colors correspond to different liquids. Green: DW, blue: RIM, orange: Gly70, red: glycerol.

5 Summary and Conclusion

A validation study on the liquid bridge stretching is presented. The experiments are performed using a high-speed video system. The axisymmetric (wedge) case is simulated using an OpenFOAM-based VOF solver, interFlow [23]. The lower substrate of the domain is numerically modeled by imposing the flow field $\mathbf{v}_d^+ = \mathbf{a} \cdot t$ at every time step. The experiments and simulations consider a wide range of Ohnesorge numbers from

10×10^{-3} to 3.8, and accelerations of the lower substrate from 0.25 to 150 m s^{-2} .

The evolution of the bridge diameter is accurately captured by the simulations. During the early stretching stage at high acceleration, the simulation results of the evolution of the bridge diameter agree very well with the experimental results. The study also investigated the symmetry of the stretching liquid bridge, and it is observed that for a lower acceleration, the liquid volume on the lower substrate is more than on the upper substrate and vice versa. The fluid viscosity also influences this effect, i.e., the increase in viscosity results in reversing the symmetry factor S of the liquid bridge.

The simplified numerical model of the lower substrate presented in this work shows very good agreement with the experimental results for a range of application parameters, i.e., $Re \geq 10$, $Oh \geq 0.001$, and $Ca \geq 0.01$. However, the numerical results deviate from the experimental results at a lower Reynolds number, i.e., $Re < 10$. Hence, the presented simplified model needs to be improved to capture these cases properly.

Acknowledgment

The authors acknowledge the financial support by the German Research Foundation (DFG) within the Collaborative Research Centre 1194 (Project-ID 265191195), projects A03, B01, and Z-INF. The use of the high-performance computing resources of the Lichtenberg High-Performance Cluster at the TU Darmstadt is gratefully acknowledged. Open access funding enabled and organized by Projekt DEAL. [Correction added on July 26, 2023, after first online publication: Projekt Deal funding statement has been added.]

The authors have declared no conflict of interest.

Symbols used

\mathbf{a}	$[\text{m s}^{-2}]$	acceleration
Ca	$[-]$	capillary number
\mathbf{g}	$[\text{m s}^{-2}]$	gravitational acceleration
\mathbf{n}_Σ	$[-]$	interface normal
Oh	$[-]$	Ohnesorge number
Re	$[-]$	Reynolds number
t	$[\text{s}]$	time
V_f^α	$[-]$	phase-specific fluxed volume

Greek letters

α	$[-]$	volume fraction
μ	$[\text{kg m}^{-1} \text{s}^{-1}]$	viscosity
\mathbf{v}	$[\text{m s}^{-1}]$	velocity
ρ	$[\text{kg m}^{-3}]$	density
σ	$[\text{N m}^{-1}]$	surface tension
χ	$[-]$	phase-indicator function
Ω_c	$[-]$	computational domain cell (control volume)
$\partial\Omega_c$	$[-]$	computational domain cell boundary

∇_c	$[-]$	discrete unstructured finite volume least squares gradient
------------	-------	--

Sub- and superscripts

\perp	normal component
\parallel	tangential component

Abbreviations

ALE	arbitrary Lagrangian-Eulerian
BIM	boundary integral method
FEM	finite element method
VOF	volume of fluid

References

- [1] X. Zhang, R. S. Padgett, O. A. Basaran, *J. Fluid Mech.* **1996**, 329, 207–245. DOI: <https://doi.org/10.1017/S0022112096008907>
- [2] L. Rayleigh, *Proc. R. Soc. London* **1878**, 10, 4. <https://www.jstor.org/stable/113853>
- [3] J. Stephen, *Ann. Phys.* **1875**, 230 (2), 316–318.
- [4] S. Kumar, *Annu. Rev. Fluid Mech.* **2015**, 47, 67–94. DOI: <https://doi.org/10.1146/annurev-fluid-010814-014620>
- [5] S. Brulin, I. V. Roisman, C. Tropea, *J. Fluid Mech.* **2020**, 899, A1. DOI: <https://doi.org/10.1017/jfm.2020.422>
- [6] S. Brulin, C. Tropea, I. V. Roisman, *Colloids Surf., A* **2020**, 587, 124271. DOI: <https://doi.org/10.1016/j.colsurfa.2019.124271>
- [7] S. Brulin, Hydrodynamic investigations of rapidly stretched liquid bridges, *Ph.D. Thesis*, TU Darmstadt **2021**.
- [8] P. Brumm, H. M. Sauer, E. Dörsam, *Colloids Interfaces* **2019**, 3, 37. DOI: <https://doi.org/10.3390/colloids3010037>
- [9] P. Brumm, T. E. Weber, H. M. Sauer, E. Dörsam, *J. Print Media Technol. Res.* **2021**, 10, 81–93. DOI: <https://doi.org/10.1088/1748-605X/ac6b06>
- [10] S. Hoath, W.-K. Hsiao, I. Hutchings, T. Tuladhar, *Phys. Fluids* **2014**, 26, 101701. DOI: <https://doi.org/10.1063/1.4897238>
- [11] B. Adhikari, T. Howes, B. Bhandari, V. Truong, *Int. J. Food Prop.* **2001**, 4, 1–33. DOI: <https://doi.org/10.1081/JFP-100002186>
- [12] K. Dhanalakshmi, S. Ghosal, S. Bhattacharya, *Crit. Rev. Food Sci. Nutr.* **2011**, 51, 432–441. DOI: <https://doi.org/10.1080/10408391003646270>
- [13] L. N. Jimenez, C. D. Martínez Narváez, V. Sharma, *Phys. Fluids* **2020**, 32, 012113. DOI: <https://doi.org/10.1063/1.5128254>
- [14] X. Wei, J. Zou, *J. Phys. Conf. Ser.* **2021**, 1888, 012014. DOI: <https://doi.org/10.1088/1742-6596/1888/1/012014>
- [15] Y. Chen, W. Gao, C. Zhang, Y. Zhao, *Lab Chip* **2016**, 16, 1332–1339. DOI: <https://doi.org/10.1039/C6LC00186F>
- [16] G. H. McKinley, T. Sridhar, *Annu. Rev. Fluid Mech.* **2002**, 34 (1), 375–415. DOI: <https://doi.org/10.1146/annurev.fluid.34.083001.125207>
- [17] J. Zhuang, Y. S. Ju, *Langmuir* **2015**, 31 (37), 10173–10182. DOI: <https://doi.org/10.1021/acs.langmuir.5b02102>
- [18] J. Donea, A. Huerta, J. P. Ponthot, A. Rodríguez-Ferran, Arbitrary Lagrangian-Eulerian Methods, in *Encyclopedia of*

- Computational Mechanics*, John Wiley & Sons, New York **2004**.
- [19] S. Dodds, M. Carvalho, S. Kumar, *Phys. Fluids* **2011**, 23 (9), 092101. DOI: <https://doi.org/10.1063/1.3623427>
- [20] S. Gaudet, G. H. McKinley, H. A. Stone, *Phys. Fluids* **1996**, 8 (10), 2568–2579. DOI: <https://doi.org/10.1063/1.869044>
- [21] *OpenFOAM: User Guide v2006*, OpenCFD, London **2006**. <https://openfoam.com/documentation/guides/latest/doc/>
- [22] *OpenFOAM-v2212*, OpenCFD, London **2022**. <https://develop.openfoam.com/Development/openfoam/-/tree/OpenFOAM-v2212>
- [23] H. Scheufler, J. Roenby, *TwoPhaseFlow: An OpenFOAM based framework for development of two phase flow solvers*, arXiv **2021**. DOI: <https://doi.org/10.48550/arXiv.2103.00870>
- [24] H. Scheufler, *TwoPhaseFlow*, GitHub, San Francisco, CA **2022**. <https://github.com/DLR-RY/TwoPhaseFlow/tree/of2206>
- [25] H. Scheufler, J. Roenby, *J. Comput. Phys.* **2019**, 383, 1–23. DOI: <https://doi.org/10.1016/j.jcp.2019.01.009>
- [26] J. Roenby, H. Bredmose, H. Jasak, *R. Soc. Open Sci.* **2016**, 3 (11), 160405. DOI: <https://doi.org/10.1098/rsos.160405>
- [27] C. Weickgenannt, I. V. Roisman, C. Tropea, *New J. Phys.* **2015**, 17 (8), 083059. DOI: <https://doi.org/10.1088/1367-2630/17/8/083059>
- [28] P. Brockmann, J. Hussong, *Exp. Fluids* **2021**, 62 (1), 23. DOI: <https://doi.org/10.1007/s00348-020-03120-4>
- [29] N. B. Vargaftik, B. N. Volkov, L. D. Voljak, *J. Phys. Chem. Ref. Data* **1983**, 12 (3), 817–820. DOI: <https://doi.org/10.1063/1.555688>
- [30] J. Kestin, M. Sokolov, W. A. Wakeham, *J. Phys. Chem. Ref. Data* **1978**, 7 (3), 941–948. DOI: <https://doi.org/10.1063/1.555581>
- [31] N. S. Cheng, *Ind. Eng. Chem. Res.* **2008**, 47 (9), 3285–3288. DOI: <https://doi.org/10.1021/ie071349z>
- [32] A. Volk, C. J. Kähler, *Exp. Fluids* **2018**, 59 (5), 75. DOI: <https://doi.org/10.1007/s00348-018-2527-y>
- [33] K. Takamura, H. Fischer, N. R. Morrow, *J. Pet. Sci. Eng.* **2012**, 98, 50–60. DOI: <https://doi.org/10.1016/j.petrol.2012.09.003>
- [34] T. Marić, D. B. Kothe, D. Bothe, *J. Comput. Phys.* **2020**, 420, 109695. DOI: <https://doi.org/10.1016/j.jcp.2020.109695>
- [35] M. H. Asghar, M. Fricke, D. Bothe, T. Maric, *Numerical wetting benchmarks – advancing the plicRDF-isoAdvector unstructured Volume-of-Fluid (VOF) method*, arXiv **2023**. DOI: <https://doi.org/10.48550/arXiv.2302.02629>
- [36] S. J. Cummins, M. M. Francois, D. B. Kothe, *Comput. Struct.* **2005**, 83 (6–7), 425–434. DOI: <https://doi.org/10.1016/j.compstruc.2004.08.017>
- [37] M. H. Asghar, P. Brockmann, X. Dong, M. Niethammer, T. Marić, I. Roisman, D. Bothe, DOI: <https://doi.org/10.48328/tudatalib-1198>
- [38] M. H. Asghar, P. Brockmann, X. Dong, M. Niethammer, T. Marić, I. Roisman, D. Bothe, DOI: <https://doi.org/10.48328/tudatalib-1199>
- [39] M. H. Asghar, T. Marić, *plicRDF-isoAdvector benchmarks for wetting processes*, **2023**. <https://github.com/CRC-1194/b01-wetting-benchmark/tree/master/LiquidBridgeStretching>, Last accessed on 2023-07-15.